Approximation of the Flow Field in Electrochemical Machining Incorporating Pressure Drop Calculation

R. Paul[1], M. Hackert-Oschätzchen[1], M. Zinecker[1], A. Schubert[1]
1. Professorship Micromanufacturing Technology, Chemnitz University of Technology, 09107 Chemnitz, Germany

Introduction

Electrochemical Machining (ECM) is a non-conventional machining technology which allows for surface structuring and shaping of metallic workpieces with high accuracy and surface quality. The machining principle of ECM is electrolysis. Hence, the mechanical properties of the workpiece material do not directly influence the machining process. Thus, even very hard materials can be machined with nearly no wear of the tool electrode. The major challenge in applying ECM is the process design. In today's practice, this is a time-consuming and cost-intensive procedure.

However, the efficiency of process design may be enhanced by simulation-based optimization. The objective function can be defined on the basis of the simulated workpiece shape. Then, for each evaluation of the objective function the resulting workpiece shape needs to be simulated. From this follows that there is a need for efficient ECM simulation models with low computational costs.

In a previous work [1] an ECM simulation model was developed, which encompassed the physical phenomena electrodynamics, fluid dynamics, thermodynamics, the formation and transport of hydrogen bubbles as well as geometry deformation. Fluid dynamics was regarded as a compressible two-phase potential flow. The pressure field was calculated based on Bernoulli's equation. The pressure drop was a model input parameter. The local total pressure was computed based on this input parameter.

In the present study the multiphysical model of the previous work [1] is revisited and extended. In particular, the submodel for computing the total pressure is replaced by a new submodel incorporating the approximation of the pressure drop for 2D ECM simulations. This submodel is built up orientated on a 1D flow model of Kozak [2]. The total pressure is regarded as a field variable that is calculated using a partial differential equation. In this equation the drop in total pressure is incorporated as a source term. The source term is defined as a function of the local Reynolds number, the local working distance between tool and workpiece and the average density and velocity in the flow cross-section. In this connection the computation of the local working distance and the averaging of local quantities across the flow cross-section is conducted by using several additional linear partial differential equations.

Theory

The approach for reducing the numerical effort of ECM simulations incorporating fluid dynamics regarded in this work is handling the fluid flow as a potential flow. This means that the fluid is regarded as inviscid and the flow field as irrotational. The two-phase flow field in the working gap is approximated by the following set of equations.

$$\frac{\partial \varrho}{\partial t} + \nabla \cdot (\varrho \nabla \phi) = 0 \tag{1}$$

$$\varrho := \phi_{\mathrm{El}}\, \varrho_{\mathrm{El}} + \phi_{\mathrm{H2}}\, \varrho_{\mathrm{H2}}(p, T_{\mathrm{ref}}) \tag{2}$$

$$\frac{\partial \phi_{\mathrm{H2}}\, \varrho_{\mathrm{H2}}}{\partial t} + \nabla \cdot (\phi_{\mathrm{H2}}\, \varrho_{\mathrm{H2}} \nabla \phi) = \nabla \cdot (\nu_{\mathrm{K}}\, \varrho_{\mathrm{H2}}\, \nabla \phi_{\mathrm{H2}}) \tag{3}$$

$$\frac{\bar{\varrho}}{2} \overline{|\nabla \phi|}^{2} + p = p_{\mathrm{tot}} \tag{4}$$

Equation (1) originates from the continuity equation and models the flow field with the flow potential ϕ and flow velocity $\vec{u} = \nabla \phi$. Moreover, equation (2) defines the density ϱ of the bubbly flow, where ϱ_{El} and $\varrho_{\mathrm{H2}}(p, T_{\mathrm{ref}})$ are the density of pure electrolyte solution and the barotropic density of hydrogen at a reference temperature T_{ref}, respectively. Equation (3) models advective and pseudo turbulent hydrogen mass transport. Here, ϕ_{H2} is the volume fraction of hydrogen. The volume fraction of electrolyte is calculated according to $\phi_{\mathrm{El}} = 1 - \phi_{\mathrm{H2}}$. The pseudo turbulent diffusion coefficient is set to $\nu_{\mathrm{K}} = 10^{-6}$ m²/s, which is based on a comparison of the potential flow model with a k-ε turbulent bubbly flow model [3]. The static pressure p required for hydrogen density calculation is computed with Bernoulli's equation (4). In this equation the bars denote the averaging over the flow cross-section. Except for this averaging, up to this point, the flow model is identical with the one used in the previous work [1] where the total pressure p_{tot} was calculated based on the streamline length. In contrast, in the

present work the goal is to model p_{tot} according to the 1D model of Kozak [2] using

$$p_{\mathrm{in}} - p_{\mathrm{out}} \coloneqq \lambda(Re)\ \frac{L}{2\,S}\,\frac{\varrho}{2}\,u^2 \tag{5}$$

$$\lambda(Re) \coloneqq \begin{cases} 96/Re & \text{if } Re < 2000 \\ 0.316/Re^{1/4} & \text{else} \end{cases} \tag{6}$$

with the width S and length L of the working gap as well as the Reynolds number Re. Since these three quantities vary within the fluid domain, equation (5) is transformed into a differential form.

$$\frac{\mathrm{d}p_{\mathrm{tot}}}{\mathrm{d}l_{\mathrm{r}}} \coloneqq \lambda(Re)\ \frac{1}{2\,S}\,\frac{\bar{\varrho}}{2}\,\bar{u}^2 \tag{7}$$

Again, the bars denote the averaging over the flow cross-section. The Reynolds number is given by

$$Re = \frac{2\,S\,\bar{\varrho}\,\bar{u}}{\mu} \tag{8}$$

where the dynamic viscosity is defined as constant. In order to compute the width of the working gap and the required averages, the flow cross-section is defined by a normed auxiliary vector field $\vec{v}_\perp$. In 2D the components of the flow field $\vec{u}$ can be used for this.

$$\vec{v}_\perp \coloneqq \frac{1}{|\vec{u}|}\begin{pmatrix} -u_y \\ u_x \end{pmatrix} \quad \text{or} \quad \vec{v}_\perp \coloneqq \frac{1}{|\vec{u}|}\begin{pmatrix} u_y \\ -u_x \end{pmatrix} \tag{9}$$

In the following, a configuration is regarded for which $\vec{v}_\perp = \vec{n}$ on the anode surface and $\vec{v}_\perp = -\vec{n}$ on the cathode surface. Here, the normal vector $\vec{n}$ points into the fluid domain.
In what follows, the width of the working gap S, also referred to as working distance, is defined as the length of the streamlines of $\vec{v}_\perp$ connecting anode and cathode. In figure 1 these streamlines are dashed and colored in red.

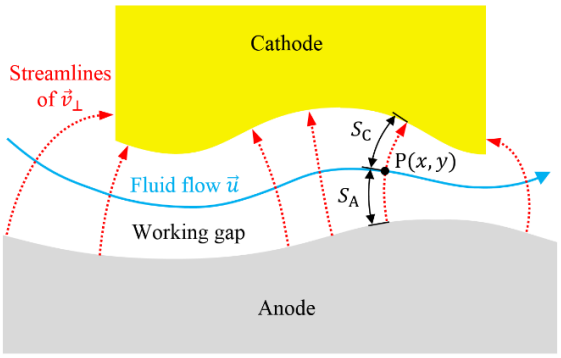

Figure 1. Working distance $S = S_{\mathrm{A}} + S_{\mathrm{C}}$ in an arbitrary point P as the length of the corresponding streamline of the auxiliary vector field $\vec{v}_\perp$

In the figure the partial lengths S_{A} and S_{C} are defined. The sum of both yields the working distance S.

$$S = S_{\mathrm{A}} + S_{\mathrm{C}} \tag{10}$$

In the following, equations for the calculation of S_{A} and S_{C} are derived. Figure 1 suggests that S_{A} is defined for any point P in the fluid domain. That is, S_{A} is a scalar field. Its gradient ∇S_{A} shall amount 1 in the direction of $\vec{v}_\perp$. This means that for these vectors $\vec{v}_\perp \cdot \nabla S_{\mathrm{A}} = 1$ must hold. The addition of a diffusion term yields the following partial differential equation.

$$\vec{v}_\perp \cdot \nabla S_{\mathrm{A}} - \nabla \cdot (s_{\mathrm{D}}\,\nabla S_{\mathrm{A}}) = 1 \tag{11}$$

The diffusion coefficient s_{D} should be chosen large enough to provide numerical stability but as small as possible to avoid undesirable spatial averaging. In this work s_{D} is set to half the local mesh size $h/2$. On the right hand side 1 acts as a source term that controls the accumulation of length. Equation (11) is solved using a Dirichlet boundary condition on the anode surface with $S_{\mathrm{A}} = 0$. At the remaining boundaries of the fluid domain the diffusive flux is set to zero. Then, S_{A} can be interpreted as the distance from the anode surface along $\vec{v}_\perp$. Similarly, the distance S_{C} from the cathode surface along $-\vec{v}_\perp$ can be computed as follows.

$$-\vec{v}_\perp \cdot \nabla S_{\mathrm{C}} - \nabla \cdot (s_{\mathrm{D}}\,\nabla S_{\mathrm{C}}) = 1 \tag{12}$$

Equation (12) is solved using the Dirichlet boundary condition $S_{\mathrm{C}} = 0$ at the cathode surface.
The source term 1 on the right hand side of equation (11) can be interpreted as the differential change of S_{A} along the direction $\vec{v}_\perp$. Disregarding the diffusion term, solving equation (11) is similar to calculating line integrals of the source term 1 along $\vec{v}_\perp$ from the anode surface to the regarded position. This motivates to calculate the average of quantities in the flow cross-section with a similar approach. For some quantity X the average $\bar{X}$ over the flow cross-section is defined according to

$$\bar{X} \coloneqq \frac{X_{\mathrm{A}} + X_{\mathrm{C}}}{S} \tag{13}$$

$$\vec{v}_\perp \cdot \nabla X_{\mathrm{A}} - \nabla \cdot (s_{\mathrm{D}}\,\nabla X_{\mathrm{A}}) = X \tag{14}$$

$$-\vec{v}_\perp \cdot \nabla X_{\mathrm{C}} - \nabla \cdot (s_{\mathrm{D}}\,\nabla X_{\mathrm{C}}) = X. \tag{15}$$

Again, the proper homogeneous Dirichlet boundary conditions are defined at the surfaces of anode and cathode, respectively. This averaging is conducted for the flow velocity magnitude $u = \sqrt{\nabla\phi \cdot \nabla\phi}$ and the density ϱ to compute the local Reynolds number and

the term $\mathrm{d}p_{\mathrm{tot}}/\mathrm{d}l_{\mathrm{r}}$ from equation (7). Subsequently, the latter term is used as a source term to calculate the local total pressure by

$$-\left(\frac{\vec{u}}{|\vec{u}|}\right)\cdot\nabla p_{\mathrm{tot}}-\nabla\cdot\left(s_{\mathrm{D}}\,\nabla p_{\mathrm{tot}}\right)=\frac{\mathrm{d}p_{\mathrm{tot}}}{\mathrm{d}l_{\mathrm{r}}} \qquad (16)$$

with a Dirichlet boundary condition $p_{\mathrm{tot}}=p_{\mathrm{out}}$ at the outlet boundary. The reader should note that in this definition p_{out} is the total pressure at the outlet, not the static pressure. Equation (16) is again motivated by the idea that this is similar to the calculation of line integrals of the right hand side, along the streamlines of $-\vec{u}$ from the outlet boundary to the regarded position.

Model Description

The design concept of the pulsed electrochemical machining process (PECM) regarded in this work is shown in figure 2. It is equivalent to the one regarded in the previous work [1].

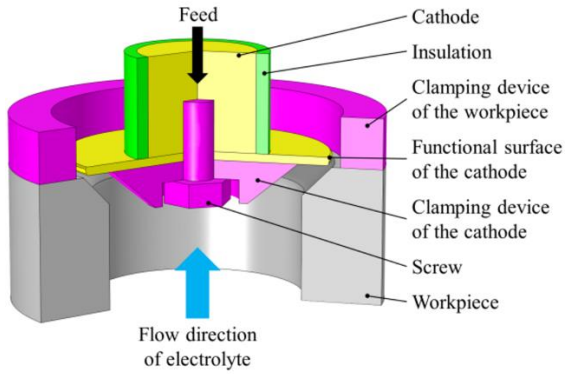

Figure 2. Design concept for machining internal precision geometries with pulsed electrochemical machining [1]

This machining process is axisymmetric. The workpiece has a predrilled bore with a diameter of 25 mm. The edge of the bore features a chamfer of 3.5 mm × 45°. The maximum diameter of the cathode disk with the functional surface is ca. 31.6 mm. Electrolyte flushing is performed from below and during machining the cathode unit is moved downwards with a constant velocity of 1 mm/min. The 2D axisymmetric model geometry derived from this design concept is shown in figure 3. Domain I represents the two-phase fluid of the bubbly flow of aqueous sodium nitrate solution and gaseous hydrogen. Domain II is the workpiece and Domain III the cathode. The workpiece is made from a powder-metallurgical steel referred to as SAM 10 and the cathode material is stainless steel 1.4301.

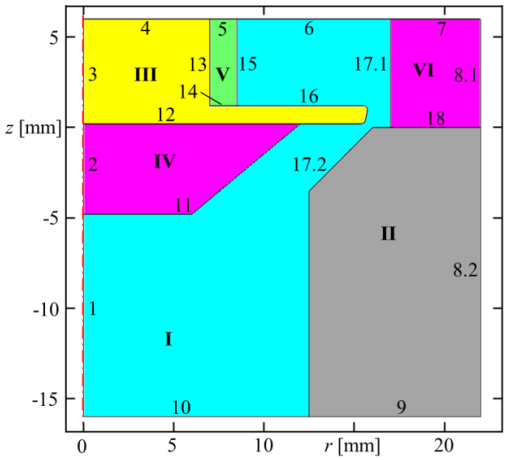

Figure 3. 2D axisymmetric geometry of the model containing the numbering of domains and boundaries at initial time t = 0 s [1]

Domains IV and V represent a clamping element and an electrical insulation element, which are both made from POM. Domain VI is the workpiece clamping element made from 1.4301. The respective material properties are listed in table 1.

Table 1: Material properties

Domain	ϱ [kg/m³]	σ [S/m]	λ [W/(m·K)]	c_p [J/(kg·K)]
I	$\varrho(\phi_{\mathrm{El}},T_{\mathrm{ref}})$	$\sigma_{\mathrm{eff}}(\phi_{\mathrm{El}},T)$	0.599	3877
II	7600	$1.69\cdot10^{6}$	21.5	410
III, VI	7900	$1.37\cdot10^{6}$	15	500
IV, V	1410	10^{-10}	0.31	1500

Here, λ is the thermal conductivity, c_p the heat capacity and σ the electrical conductivity. The electrical conductivity of the fluid is defined as a function of the electrolyte volume fraction and the temperature. [1]

$$\sigma_{\mathrm{eff}}(\phi_{\mathrm{El}},T):=\left(A\left(\frac{T}{1\mathrm{K}}-273.15\right)+B\right)\cdot\phi_{\mathrm{El}}^{\frac{3}{2}} \qquad (17)$$

The parameters were set to $A=1.646$ mS/cm and $B=39.796$ mS/cm. According to this equation the electrical conductivity of the fluid increases linearly with temperature and nonlinearly with electrolyte volume fraction. The reference temperature for the hydrogen density calculation was set to $T_{\mathrm{ref}}=20$ °C. Furthermore, for the calculation of the Reynolds number the viscosity of the fluid was defined to amount $\mu=1.042$ mPa·s.
In the regarded pulsed electrochemical machining process current pulses are applied. The cathode unit is moved towards the workpiece with a constant feed velocity. This is illustrated in figure 4.

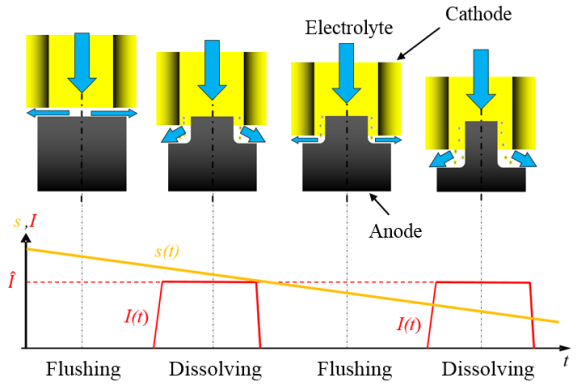

Figure 4. Electrical current pulses $I(t)$ and cathode feeding path $s(t)$ in pulsed electrochemical machining (PECM) without cathode oscillation [4]

Schaarschmidt et al. [5] presented a comprehensive modelling method for PECM in which the current pulses are simulated in a multiscale approach. This is even applicable to PECM processes with cathode oscillation. However, for the sake of comparability with the previous work [1] electrodynamics is modeled using a pseudo direct current approach. This means that temporally constant boundary conditions are applied. The simulated electric current $\hat{I}$ corresponds to the real electric current during pulse-on time, as depicted in figure 4. In what follows, the hat above the symbol denotes pseudo direct current related quantities. The pulsation of the electric current is characterized by the duty cycle c_I.

$$c_I = t_{\mathrm{on}} \cdot f_{\mathrm{P}} \tag{18}$$

Here, t_{on} is the pulse-on time and f_{P} is the pulse frequency. The process parameters regarded in this work are summarized in table 2. For the purpose of comparability the process parameter values equal the ones used in the previous work [1].

Table 2: Process parameters, equal to previous work [1]

Parameter	Symbol	Value
Feed velocity	v_{f}	1 mm/min
Electric process voltage during pulse-on time	$\hat{U}$	14 V
Duty cycle	c_I	0.8
Electrolyte volume flow rate	$\dot{V}_{\mathrm{El}}$	8 l/min
Absolute total pressure at flow outlet	p_{out}	5.5 bar
Ambient temperature	T_{A}	20 °C

The numerical model was built up in COMSOL Multiphysics using the Physics Interfaces Electric Currents, Heat Transfer in Fluids, General Form PDE, Coefficient Form PDE and Deformed Geometry. The boundary conditions of electrodynamics are given in table 3. In the following, the numbering of domains and boundaries refers to the definition from figure 3.

Table 3: Electrodynamical boundary conditions

Label	Boundary	Details
Axial Symmetry	1 – 3	–
Electric Insulation	5 – 7, 9, 10	$\vec{n} \cdot \hat{\vec{J}} = 0$
Ground	4	$\hat{\varphi} = 0$
Electric Potential	8.1, 8.2	$\hat{\varphi} = \hat{U} - U_{\mathrm{O}}$ $U_{\mathrm{O}} = 6$ V

Here, $\hat{\vec{J}}$ is the electric current density during pulse-on time, $\hat{\varphi}$ is the respective electric potential, and U_{O} is the electrochemical overpotential that occurs at the electrolyte-electrode interfaces. In this work U_{O} is considered to be constant and constantly partitioned on both electrode-electrolyte interfaces. Hence, this potential drop can be taken in account by subtraction from the electric process voltage. The value $U_{\mathrm{O}} = 6$ V was chosen based on experimental results. The boundary conditions of thermodynamics are defined in table 4.

Table 4: Thermodynamical boundary conditions

Label	Boundary	Details
Axial Symmetry	1 – 3	–
Thermal Insulation	5, 7, 9	$\vec{n} \cdot \vec{q} = 0$
Temperature	4, 8.1, 8.2, 10	$T = T_{\mathrm{A}}$
Outflow	6	$\vec{n} \cdot \vec{q} = 0$
Boundary Heat Source Anode	17.1, 17.2	$Q_{\mathrm{b}} = (U_{\mathrm{O}} - 1\ \mathrm{V})\ \lvert\hat{J}_n\rvert$
Boundary Heat Source Cathode	16	$Q_{\mathrm{b}} = 1\ \mathrm{V}\ \lvert\hat{J}_n\rvert$

Here, $\vec{q}$ is the heat flux density, T the temperature, Q_{b} the boundary heat source and $\hat{J}_n$ is the normal electric current density. According to the table the cathodic overpotential is considered to amount 1 V and the anodic overpotential $U_{\mathrm{O}} - 1$ V. Furthermore, Joule heating is regarded in both fluid and solid domains.
Fluid dynamics is modeled according to the derivations of the previous chapter. The subjects and solution variables of the equations of fluid dynamics are summarized in table 5.

Table 5: Subjects and solution variables of fluid dynamics

Subject	Solution variable	Equation
Mass conservation	ϕ	1
Density of the dispersion	ϱ	2
Hydrogen transport	ϕ_{H2}	3
Static pressure	p	4
Friction factor	λ	6
Pressure drop	$\mathrm{d}p_{\mathrm{tot}}/\mathrm{d}l_{\mathrm{r}}$	7
Reynolds number	Re	8
Auxiliary vector field	$\vec{v}_{\perp}$	9
Working distance	S (S_{A}, S_{C})	10 – 12
Cross-section averages	$\bar{u}$ (u_{A}, u_{C}) & $\bar{\varrho}$ (ϱ_{A}, ϱ_{C})	13 – 15
Total pressure	p_{tot}	16

At the cathode surface hydrogen production $\Phi_{\mathrm{H2,n}}$ is modeled according to Faraday's law

$$\Phi_{\mathrm{H2,n}} = -\frac{M_{\mathrm{H2}}}{2\,F}\hat{J}_n \qquad (19)$$

where M_{H2} is the molar mass of hydrogen and F is Faraday's constant.

The reader should note that in the regarded case of an 2D axisymmetric model, the proper equation form in cylindrical coordinates has to be applied. With equations describing the conservation of thermodynamical quantities this leads to additional source terms. However, with the equations for the working distance this is not the case, since 1D geometric quantities are described. Here, the 2D and 2D axisymmetric equation forms equal. Moreover, in this work the cross-section averages were treated in the same way. This means that these can rather be interpreted as line averages.

Transient material removal and the tool feed movement were modeled using Deformed Geometry. The Free Deformation domain condition is defined in domains I – V and Fixed Mesh is defined in domain VI. The Boundary conditions of geometry deformation are listed in table 6.

Table 6: Geometry deformation boundary conditions

Label	Boundary	Details
Prescribed Mesh Displacement rz	4 – 6, 8.2, 17.1, 18	$d_r = 0$ $d_z = 0$
Prescribed Mesh Displacement r	1 – 3, 13, 15	$d_r = 0$
Prescribed Mesh Displacement z	9, 10	$d_z = 0$
Prescribed Mesh Displacement Tool	2, 11, 12, 14, 16	$d_r = 0$ $d_z = -v_{\mathrm{f}}\ t$
Prescribed Mesh Velocity Removal	17.2	$v_r = n_r\ \bar{v}_{\mathrm{a,c}_I}(\hat{J}_n)$ $v_z = n_z\ \bar{v}_{\mathrm{a,c}_I}(\hat{J}_n)$

Here, d_r, d_z and v_r, v_z are the components of the displacement vector and the displacement velocity, respectively. The time-averaged material removal velocity $\bar{v}_{\mathrm{a,c}_I}(\hat{J}_n)$ was obtained from experimental results and is given by

$$\bar{v}_{a,c_I}(\hat{J}_n) = \begin{cases} 0 & \text{if } \hat{J}_n < 11\,\frac{\mathrm{A}}{\mathrm{cm}^2} \\ C\,\hat{J}_n - D & \text{else} \end{cases} \qquad (20)$$

where for the corresponding constants the values were defined to be $C = 0.0123$ (cm²/A)·(mm/min) and $D = 0.1353$ mm/min.

Simulation Results

The pulsed electrochemical machining process was simulated for a maximum process time of $t = 250$ s. In what follows, crucial simulation results at $t = 250$ s are presented. Figure 5 shows streamlines of the flow field. The streamline color represents the flow velocity magnitude.

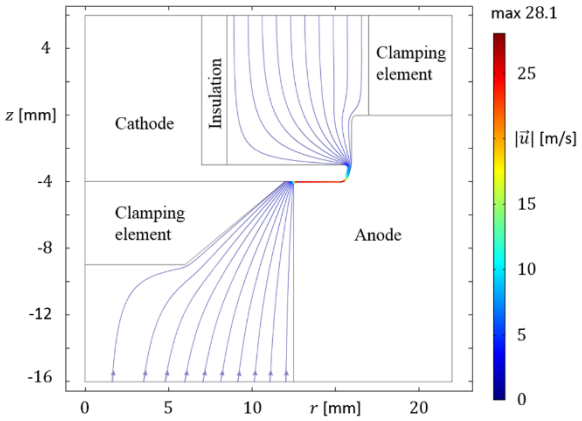

Figure 5. Streamlines of the flow field $\vec{u}$ at $t = 250$ s, color represents flow velocity magnitude

The electrolyte enters the fluid domain at the lower model boundary as depicted by arrows on the streamlines. At the entrance of the working gap the flow velocity increases significantly, which is due to the decreased area of the flow cross-section. In the working gap the flow velocity slightly declines with increasing radius r since the area of the flow cross-section increases. It decreases further in the lateral working gap. After exiting the working gap the fluid flows off well-ordered and uniformly distributed on the flow cross-section.

The working distance S is shown in figure 6 with a logarithmic scale. Furthermore, streamlines of the auxiliary vector field $\vec{v}_{\perp}$ are plotted.

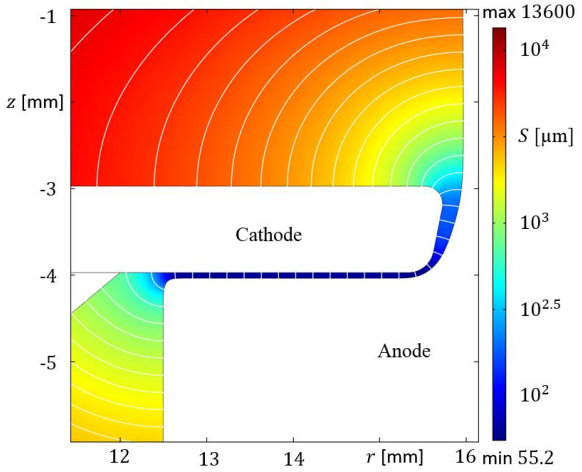

Figure 6. Working distance S at $t = 250$ s, streamlines represent auxiliary vector field $\vec{v}_\perp$

In the developed model these lines represent flow cross-sections. In the front working gap S amounts 65 µm ± 2 µm which is in agreement with 65 µm. The minimum values of S are found at the transition to the lateral working gap and amount 58 µm ± 2 µm. This is also in agreement with the actual geometric dimension of ca. 58 µm. Furthermore, it can be found that the values on and in the immediate vicinity of the boundaries are ca. 5 % lower than the values in the bulk of the nearby fluid domain. This may be due to the choice of boundary conditions.
In figure 7 a comparison of the flow velocity magnitude $u = |\vec{u}|$ and the cross-sectional average $\bar{u}$ is shown.

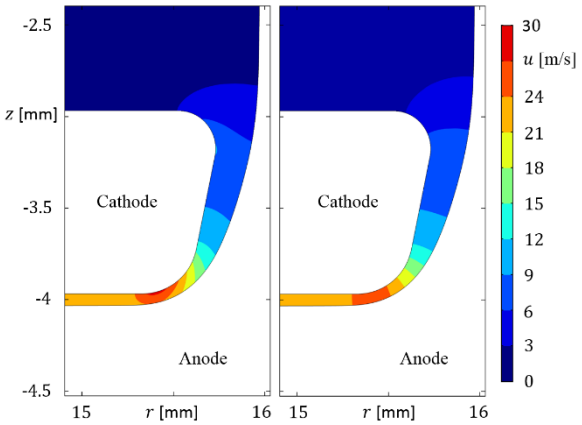

Figure 7. Comparison of the flow velocity magnitude u (left) and the cross-sectional average $\bar{u}$ (right) at $t = 250$ s

In the figure on the left it can be seen that the maximum velocity magnitude occurs at the lower edge of the cathode. There, the velocity distribution across the flow cross-section is non-uniform. In the figure on the right the cross-sectional velocity average calculated with equations (13) to (15) is shown. Obviously, the distribution of $\bar{u}$ across the flow cross-section defined by $\vec{v}_\perp$ is approximately uniform.
The local Reynolds number Re is plotted in Figure 8. The scale is restricted to range of 2600 to 4400. In some parts of the fluid domain significantly higher values are achieved.

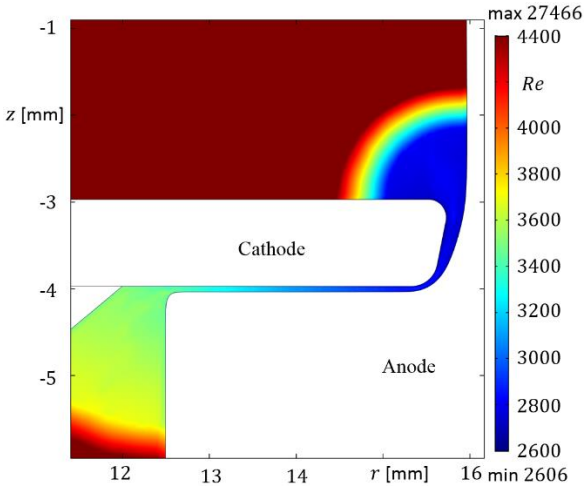

Figure 8. Local Reynolds number Re at $t = 250$ s

However, these values have only marginal influence on the pressure drop calculation due to the corresponding high S and low u, respectively. At the entrance of the working gap the local Reynolds number amounts ca. 3400. Due to the increasing radius and cross-sectional area, the Reynolds number drops along the working gap to approximately 3750 in the bulk of the fluid. In the upper part of figure 9 the calculated static pressure p is shown for the presented potential flow model. Furthermore, for the same geometry the result of a stationary simulation with the turbulent two-phase bubbly flow model presented in a previous work [3] is shown in the lower figure.

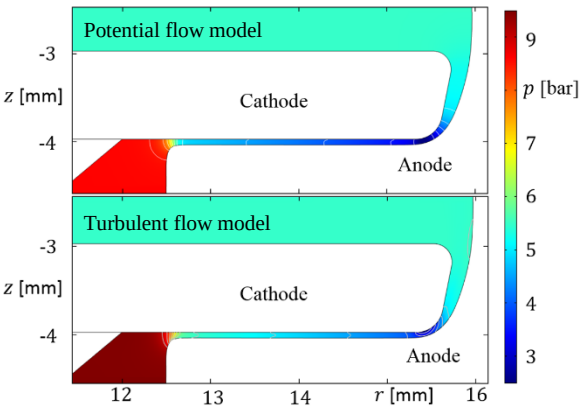

Figure 9. Static pressure p at $t = 250$ s (above) and static pressure for the simulated geometry at $t = 250$ s computed with the turbulent two-phase bubbly flow model presented by Hackert-Oschätzchen [3] (below)

In the chamber below the cathode, due to the low flow velocity the static pressure is almost equal to the total pressure at the fluid inlet. In the case of the potential flow model this amounts 8.6 bar. At the entrance of the working gap p decreases significantly, which can be traced back to the increased flow velocity. Along the working gap p decreases further which is due to the drop in total pressure. The minimum of the static pressure of 2.5 bar occurs at the lower edge of the cathode in the area of the flow velocity maximum. While exiting the lateral working gap p increases due to the decreasing flow velocity and approaches the value of the total pressure at the outlet boundary. The overall qualitative agreement of both models is well. However, the simulated pressure drops differ. For the potential flow model the simulated pressure drop along the working gap amounts 3.13 bar. The simulation with the turbulent flow model predicts a higher pressure drop of 4 bar. The difference of the pressure of the potential flow model from the turbulent flow model is shown in figure 10.

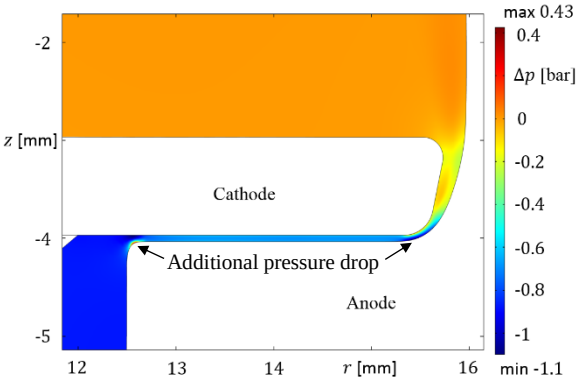

Figure 10. Difference of pressure simulated with the potential flow model from the turbulent flow model

Inside the front working gap the difference is almost constant. The differences between the models arise mainly at the entrance of the working gap and the lower edge of the cathode, which are marked in the figure. These additional pressure drops are due to the certain geometrical conditions and are not encompassed by the presented potential flow model.

Conclusions

A two-phase potential flow model for the approximation of the flow field in ECM was presented. In this work, for the potential flow model a new submodel for the approximation of the pressure drop was developed. The updated model is able to describe the influence of changes in volume flow rate and geometry on the pressure field and thus on the hydrogen volume fraction, the effective electrical conductivity, and the material removal, respectively. Despite the use of several additional partial differential equations, the numerical effort is significantly lower than with turbulent flow models. By the comparison with the results from a turbulent flow model it could be shown that the overall qualitative agreement of both models is high. However, the pressure drop predicted by the developed submodel is ca. 22 % lower. This could be traced back to the fact that in the turbulent flow at the entrance and exit of the working gap additional pressure drops occur. This may be overcome by an adaption of the pressure drop source term in the developed submodel for pressure drop calculation. Due to the model assumptions of the potential flow model complex flow structures, like eddies and flow detachments cannot be depicted. Furthermore, the no-slip boundary condition is not satisfied at the walls. Hence, the presented model can be regarded as a computationally efficient tool for process design in ECM.

References

1. M. Hackert-Oschätzchen, M. Kowalick, R. Paul, M. Zinecker, D. Kuhn, G. Meichsner, A. Schubert, 2-D Axisymmetric Simulation of the Electrochemical Machining of Internal Precision Geometries, *Proceedings of the 2016 COMSOL Conference in Munich* (2016)
2. J. Kozak, K. P. Rajurkar, B. Wei, Modelling and Analysis of Pulse Electrochemical Machining (PECM), *ASME*, 116, 316 – 323 (1994)
3. M. Hackert-Oschätzchen, R. Paul, M. Kowalick, D. Kuhn, G. Meichsner, M. Zinecker, A. Schubert, Characterization of an Electrochemical Machining Process for Precise Internal Geometries by Multiphysics Simulation, *Procedia CIRP*, 58, 175 - 180 (2017)
4. A. Schubert, G. Meichsner, M. Hackert-Oschätzchen, M. Zinecker, J. Edelmann, Pulsed Electrochemical Machining of Powder Metallurgy Steels, *Proceedings of International Symposium on Electrochemical Machining Technology - INSECT*, 68 - 75 (2011)
5. I. Schaarschmidt, M. Zinecker, M. Hackert-Oschätzchen, G. Meichsner, A. Schubert, Multiscale Multiphysics Simulation of a Pulsed Electrochemical Machining Process with Oscillating Cathode for Microstructuring of Impact Extrusion Punches, *Procedia CIRP*, 58, 257 - 262 (2017)

Acknowledgements

This project is funded by the Federal Ministry of Economics and Technology, following a decision of the German Bundestag.